Electrochemical Behavior of Tin Foil Anode in Half Cell and Full Cell with Sulfur Cathode

Yi Cui, Tianyi Li, Xinwei Zhou, Aaron Mosey, Wei Guo, Ruihua Cheng, Yongzhu Fu*, and Likun Zhu*

Y. Cui, T. Li, X. Zhou, Prof. L. Zhu

Department of Mechanical Engineering, Indiana University-Purdue University Indianapolis, Indianapolis, IN 46202, United States

*Corresponding author: likzhu@iupui.edu (L. Zhu)

Y. Cui, T. Li, X. Zhou

School of Mechanical Engineering, Purdue University, West Lafayette, IN 47907, United States

Prof. W. Guo, Prof. Y. Fu

College of Chemistry and Molecular Engineering, Zhengzhou University, Zhengzhou 450001, China

*Corresponding author: yfu@zzu.edu.cn (Y. Fu)

A. Mosey, Prof. R. Cheng

Department of Physics, Indiana University-Purdue University Indianapolis, Indianapolis, IN 46202, United States

Abstract

Tin-based (Sn) metal anode has been considered an attractive candidate for rechargeable lithium batteries due to its high specific capacity, safety and low cost. However, the large volume change of Sn during cycling leads to rapid capacity decay. To address this issue, Sn foil was used as a high capacity anode by controlling the degree of lithium uptake. We studied the electrochemical behavior of Sn foil anode in half cell and full cell with sulfur cathode, including phase transform, morphological change, discharge/charge profiles and cycling performance. Enhanced cycling performance has been achieved by limiting the lithiation capacity of the Sn foil electrode. A full cell consisting of a pre-lithiated Sn foil anode and a sulfur cathode was constructed and tested. The full cell exhibits an initial capacity of 1142 mAh g^{-1} (based on the sulfur mass in the cathode), followed by stable cycling performance with a capacity retention of 550 mAh g^{-1} after 100 cycles at C/2 rate. This study reports a potential prospect to utilize Sn and S as a combination in rechargeable lithium batteries.

1. **Introduction**

Tin-based (Sn) metal anode has attracted much attention as an alternative of graphite anode for the development of high energy density lithium ion batteries (LIBs) due to its high capacity, low cost, abundance and non-toxic property [1]. Sn has theoretical capacities of 993 mAh g^{-1} and 2094 Ah L^{-1} according to the formation of Li$_{4.4}$Sn, which are about 3 times of the capacities of graphite (372 mAh g^{-1} and 740 Ah L^{-1}) [2, 3]. However, the large volume change (260%) upon lithiation/delithiation processes leads to Sn particle fracture and electrode delamination from the current collector, which result in rapid capacity decay [4-6]. Although much effort has been made to alleviate these issues for achieving high capacity and good cycle life, such as nano-structuring Sn [7-11] and developing Sn-based composite materials [12-16], the large volume change upon cycling is still a hurdle for the practical application of Sn anode. In addition to the Sn particle-based composite electrode including binder, carbon additive and current collector, bulk Sn foil has also been used to study its crystallographic changes during lithiation/delithiation processes and understand the mechanisms of capacity fade. For instance, Rhodes et al. monitored the phase transformation behavior of sputtered Sn thin films throughout an entire lithiation/delithiation cycle using in-situ X-ray diffraction (XRD) [17]. The presence of four phases including white Sn, Li$_2$Sn$_5$, β-LiSn, and Li$_{22}$Sn$_5$ were identified. Hassoun et al. reported the preparation and characterization of various samples of metallic Sn electroplated on a copper foil under different current and time regimes [18]. Tamura et al. investigated an electrodeposited Sn layer on copper foil [19]. They found that the poor cycle life was resulted from a lack of interface strength between the entire part of the active material and the current collector. Yang et al. studied the behavior of a bulk Sn foil electrode [20]. They concluded that the poor cycle life is related to an inability to completely remove all the inserted lithium. Recently, an interdigitated

3

eutectic alloy including Sn and aluminum (Al) has been developed as a high capacity anode [21]. In this eutectic alloy, nanosized electrochemically active Sn domains are surrounded by an electrically conductive Al network, which enables stable cycling.

Bulk Sn foil electrode offers several advantages over the particle-based composite electrode, such as ease of fabrication, very high fraction of active materials and high volumetric capacity. In addition, bulk Sn foil can be easily pre-lithiated and used as the anode for LIBs, in which the cathode does not contain lithium at the charged state, such as lithium sulfur battery. There have been few studies on silicon-sulfur batteries [22-24], lead-sulfur batteries [25], and especially the Sn-sulfur batteries. Hassoun and Scrosati developed a tin sulfur LIB using Sn/C composite as the anode and Li_2S/C composite as the cathode [26]. They concluded that the use of a Sn/C composite anode eliminates the risk of shuttle effect, which is a major problem in lithium sulfur battery using a lithium metal anode. However, the Sn/C composite anode still cannot offer good cycle life due to the large volume change of Sn. It has been proposed that limiting the degree of lithium uptake in Sn could relieve the fracture problem to some extent [17]. Due to the advantage of high capacity offered by bulk Sn electrode, we hypothesize that it is possible to develop a bulk Sn foil anode with both high capacity and good cycle life by limiting the degree of lithium uptake. In commercial LIBs, the realized capacity of graphite anode is ∼150 mAh g^{-1} when the weights of the copper current collector, conductive carbon, and polymer binder are included [21]. If the lithium uptake of bulk Sn foil electrode is limited to 20%, it still has a capacity of 198 mAh g^{-1}, which is higher than the realized capacity of graphite anode. If we consider half of the volume of the graphite electrode is occupied by graphite, the

4

realized volumetric capacity is about 370 Ah L^{-1}. The capacity of bulk Sn foil electrode is 418

Ah L^{-1}, considering 20% lithium uptake.

Therefore, the objective of this paper is to investigate the electrochemical behavior of bulk

Sn foil anode in both half cell and full cell with sulfur cathode. In this work, we studied the

phase transform of Sn foil anode by analyzing ex-situ XRD data at different state of charge

during lithiation processes. A thin copper layer was sputtered on one side of the Sn foil as a

protective layer to improve electrical connection between Sn anode and the coin cell case. By

controlling the lithium concentration of the lithiation and phase transform, an enhanced cycle life

of 90 cycles can be obtained. We also incorporated the Sn foil anode with a sulfur cathode in

ether-based electrolyte as a full cell. The morphological changes at anode after cycling and the

electrochemical phenomena were studied.

2. Experimental

2.1. Materials

Tin foil (Sn, 0.025 mm thick, 99.9% (metals basis), Alfa Aesar), lithium

bis(trifluoromethanesulfonimide) (LiTFSI, LiN(CF$_3$SO$_2$)$_2$, 99%, Acros Organics), lithium nitrate

(LiNO$_3$, anhydrous, 99.999% (metals basis), Alfa Aesar), 1,2-dimethoxyethane (DME, 99.5%,

Sigma Aldrich), 1,3-dioxolane (DOL, 99.8%, Sigma Aldrich), sublimed sulfur (S$_8$, Fisher

Scientific), Super C65 (conductive carbon black, Timcal), polyvinylidene fluoride (PVdF,

Kureha Battery Materials Japan Co., Ltd.), 1-methyl-2-pyrrolidone (NMP, 99.5%, Sigma

Aldrich) and carbon disulfide (CS$_2$, Certified ACS, Fisher Scientific) were purchased and used as

received.

2.2. Electrolyte preparation

The blank electrolyte is composed of 1.0 M LiTFSI in mixture solvent of DME and DOL (1:1 v/v). The S-Sn full cell electrolyte is composed of 1.0 M LiTFSI and 0.1 M $LiNO_3$ in mixture solvent of DME and DOL (1:1 v/v).

2.3. Preparation of Sn anode and S cathode

Sn foils were polished by a piece of sandpaper (2500 grit) to remove the native oxide layer and then cleaned by Acetone for several times. One piece of the cleaned Sn foil was cut into 0.49 cm^2 discs (D = 7.9 mm, including 9.5 mg Sn each) as pristine Sn electrodes for XRD collection. Another piece of the cleaned Sn foil was covered with a copper (Cu) layer on one side of the Sn foil through magnetron sputtering deposition method. The sputtering was carried using a source target (AJA international) in a home-built high vacuum chamber. A base pressure of 10^{-6} Torr was maintained while during deposition and an inert argon atmosphere was introduced at a pressure of 10^{-3} Torr. Gas flow rate was regulated by a mass flow controller (MKS, model 250) to create and maintain a localized, steady plasma above the biased Cu target. Deposition rate was calibrated to be 0.22 nm s^{-1} using a harmonic single crystal monitor attached to the deposition chamber. Thin Cu film of ~500 nm was deposited on the Sn foil sample. Then the sputtered Sn foil was cut into 0.49 cm^2 discs for Sn half-cell test, and 0.7 cm^2 discs (D = 9.5 mm, including 13.5 mg Sn each) for pre-lithiation as the anode in S-Sn full cells. All the cut Sn foil electrodes were stored in an Ar-filled glove box.

Commercial binder-free carbon nanotube (CNT) paper called buckypaper (NanoTechLabs Composites, Inc) was used as the current collector for the sulfur electrode in this study. The CNT paper was cut into 0.49 cm^2 discs (D = 7.9 mm, about 0.9 mg each) and dried at 100 °C for 24 h in a vacuum oven before use. 1.5 M sulfur solution was prepared by adding sulfur into CS$_2$. The solution was stirred to be dissolved completely. Then 10 µL solution was added into the CNT current collector in a petri dish. The CNT current collector with S was dried in a vacuum oven at room temperature for 24 h. The mass loading of sulfur on CNT current collector is approximately 1.02 mg cm^{-2}.

2.4.   Preparation of carbon-coated separator

The Carbon-coated separator was fabricated by surface coating commercial conductive carbon black (Super C65) on one side of a commercial polypropylene separator (Celgard 2400). The carbon slurry was prepared by mixing Super C65 carbon and PVdF in NMP solvent with the ratio of 8:2 (Super C65: PVdF) for 24 h. The carbon slurry was coated onto the Celgard 2400 using a doctor blade and then dried at 35 °C for 24 h in a vacuum oven. The Carbon-coated separator was then cut into 1.77 cm^2 circular disks (D = 15 mm, Celgard 2400 mass is about 2.5 mg each, carbon mass is about 0.8 mg (0.45 mg cm^{-2})).

2.5.   Sn half-cell fabrication and electrochemical evaluation

CR2032 coin cells were used and cells were fabricated in an Ar-filled glove box. First, a stainless-steel plate was placed in coin cell case. A Sn foil electrode (0.49 cm^2) was placed on the plate and inserted into coin cell with the copper side facing down, followed by adding 10 µL blank electrolyte. Then a Celgard 2400 separator was placed on top of the Sn electrode followed

by adding another 10 μL blank electrolyte on top of the separator. Then a piece of lithium metal was placed on the separator. Finally, a stainless-steel plate covered the lithium metal with a spring as the spacer. The cell was crimped and taken out of the glove box for electrochemical evaluation.

Cells were galvanostatically cycled between 0.35 and 1.2 V on an Arbin BT2000 battery cycler at 0.03 C rate (1 C = 993 mA g^{-1}, based on the mass of Sn in the cells). The lithiation capacity limited cells were galvanostatically cycled between 0.01 and 1.2 V at 0.03 C rate with 1 mAh lithiation capacity limitation (2.04 mAh cm^{-2}). The cell for low current analysis was galvanostatically cycled at 10 μA cm^{-2}. Cyclic voltammetry (CV) was performed on a BioLogic VSP potentiostat. The potential was swept from open circuit voltage to 0.35 V and then swept back to 1.2 V at a scanning rate of 0.05 mV s^{-1}.

For XRD collection, cells were fabricated by using pristine Sn electrodes followed by the same procedure, which avoids the strong effect of copper under x-ray diffraction. These cells were galvanostatically cycled between 0.01 and 1.2 V at 0.03 C rate. Different lithiation status were collected by limiting the lithiation capacity.

2.6.   S half-cell fabrication and electrochemical evaluation

CR2032 coin cells were used and cells were fabricated in an Ar-filled glove box. First, 15 μL full cell electrolyte was added into the prepared CNT paper electrode. Then a Celgard 2400 separator was placed on top of the electrode followed by adding another 15 μL electrolyte on the separator. Finally, a piece of lithium metal and nickel foam as a spacer were placed on the

8

separator. The cell was crimped and taken out of the glove box for electrochemical evaluation.

Cells were galvanostatically cycled on an Arbin BT2000 battery cycler at 0.2 C rate (1 C = 1672

mA g^{-1}, based on the mass of sulfur in the cells). CV was performed on a BioLogic VSP

potentiostat. The potential was swept from open circuit voltage to 1.7 V and then swept back to

2.8 V at a scanning rate of 0.02 mV s^{-1}.

2.7.   Sulfur-tin (S-Sn) full cell fabrication and electrochemical evaluation

To pre-lithiate the Sn anode, a Sn (0.7 cm^2) half cell was fabricated by following the same

Sn half cell fabrication procedure shown in section 2.5. Then the cell was galvanostatically

cycled between 0.35 and 1.2 V with 1.5 mAh (2.1 mAh cm^{-2}) lithiation capacity limitation for 4

cycles. Then the cell was opened to obtain the lithiated Sn anode. To fabricate a S-Sn full cell, a

stainless-steel plate was placed in coin cell case. A sulfur cathode was placed on the plate

followed by adding 15 μL full cell electrolyte. Then a carbon-coated separator was placed on top

of the sulfur cathode and inserted into coin cells with the carbon side facing the cathode,

followed by adding another 15 μL full cell electrolyte on top of the separator. Finally, the

lithiated Sn anode was placed on the separator with a spring as the spacer. The cell was crimped

and taken out of the glove box for testing.

Cells were galvanostatically cycled between 1.1 and 2.3 V on an Arbin BT2000 battery

cycler at 0.5 C rates (1 C = 1672 mA g^{-1}, based on the mass of sulfur in the cells). CV was

performed on a BioLogic VSP potentiostat. The potential was swept from open circuit voltage to

1.1 V and then swept back to 2.3 V at a scanning rate of 0.05 mV s^{-1}.

2.8.   Characterization

The XRD data were collected on a Bruker D8 Discover XRD Instrument equipped with Cu Kα radiation. The pristine Sn foil was placed on a glass slide and protected with Kapton film. The scanning rate was 0.5° min⁻¹, and 2θ was set between 20° and 90°. The cycled Sn electrodes for XRD were obtained by opening the Sn half cells in an Ar-filled glove box. The cycled electrodes were dried under vacuum in a chamber of the glovebox for 30 min. Then the XRD samples were prepared by following the same procedure. The XRD patterns were collected under the same conditions for comparison.

The cycled Sn electrodes for scanning electron microscopy (SEM) were obtained by opening the S-Sn full cells in an Ar-filled glove box, followed by the same drying procedure. The morphological characterization of the electrodes was conducted with a JEOL JSM-7800F field emission SEM. The elemental mapping was performed with energy-dispersive X-ray spectroscopy (EDS) attached to the SEM with 7 KV.

3. Results and Discussion

The Sn foil electrode was galvanostatically cycled between 0.35 and 1.2 V at 0.03 C rate. The cycling performance is shown in **Fig. 1a**. The Sn foil electrode has an initialcapacity of 10.2 mAh cm⁻² and the capacity decreases to 2.1 mAh cm⁻² after 30 cycles. The cell has an initial Coulombic efficiency (CE) of 95%, followed by an average efficiency of >90% over 20 cycles, then the efficiency fades to 60% after 30 cycles. The electrochemical behavior was studied via CV, as shown in **Fig. 1b**. In the cathodic scan from open circuit voltage (OCV) to 0.35 V, no obvious peaks are observed until 0.4 V, at which the lithiation occurs. In the 2ⁿᵈ cycle, the

lithiation mainly occurs at 0.69 V, 0.56 V and 0.39 V. The delithiation process is reversed in the anodic scan presented by three separated peaks at 0.61 V, 0.73 V and 0.8 V, respectively. The voltage profile is shown in **Fig. 2a**, which resembles the CV. There is only one discharge voltage plateau in the first lithiation process, and there are multiple plateaus in the following cycle.

To understand the phase transformation during these processes, ex-situ XRD patterns were collected at different states of lithiation, which are shown in **Fig. 2b** and **c**. The XRD pattern of the pristine Sn foil shows strong peaks of (200), (101) and (211) planes and weaker peak of (220) plane. A continuous diminution in the Sn peak intensity is firstly observed on the first lithiation plateau (point **1-3**), followed by the presence of the Li_2Sn_5 and LiSn phases. At the end of the single lithiation plateau (point **3**), the mainly present phase is detected to be $Li_{22}Sn_5$, mixing with small parts of Li_2Sn_5 and LiSn. At the end of lithiation (point **4)**, the Sn peaks completely disappear and the XRD pattern only shows peaks of $Li_{22}Sn_5$. After the electrode was charged to 1.2 V (point **5**), the delithiated product is also scanned by XRD. It is observed that the Sn phase appears again, which is mixed with Li_2Sn_5 and LiSn meaning an incomplete delithiation process after the cell was charged to 1.2 V.

The XRD patterns of the 2nd lithiation process are shown in **Fig. 2c**. The voltage profile shows three typical plateaus, on which four scan points were collected to detect the phase changes. The four collected data are corresponding to the terminals of the three voltage plateaus and the completed lithiation stage, respectively. At the end of the 1st voltage plateau (point **6**), the decreased intensity of Sn peaks is due to depleting Sn upon lithation. The transformed phases are mainly Li_2Sn_5 and LiSn phases. At the end of the 2nd plateau (point **7**), the XRD pattern

11

shows that the Sn phase completely disappeared. Li_2Sn_5 is the mainly crystalline phase mixed with a small amount of LiSn. After the 3rd lithiation plateau (point **8**), $Li_{22}Sn_5$ phase with high intensities is shown accompanied with abridged presence of the LiSn phase. After discharging to 0.01 V (Point **9**), $Li_{22}Sn_5$ phase is the only detected crystalline lithiation phase. The morphological change from pristine Sn foil to lithiated Sn at 0.01 V is shown in **Fig. 2d**. The pristine Sn foil has a polished surface with metallic luster. When it is fully lithiated to $Li_{22}Sn_5$, the foil becomes dark black and cracked into pieces. The large volume expansion results in the pulverization of the Sn foil, which is the main reason of the contact loss and fast capacity decay. **Figs. 2e** and **f** show the crystal structure change from Sn to $Li_{22}Sn_5$. The Sn crystal initially has a cubic structure. The $Li_{22}Sn_5$ mainly adopts a Body-Centered Cubic structure [17]. The XRD results show Li_2Sn_5 and LiSn are the main transition crystalline structures. No other high degree phases of lithiation such as Li_7Sn_3, $Li_{13}Sn_5$ and Li_7Sn_2 are detected.

It is observed that the first lithiation process only has one plateau, which is different from the 2nd lithiation with three typical plateaus. The long plateau in the first lithiation has been considered as the result of disorder in the initially formed material [20]. We believe that this unique phenomenon could be due to the large difference in lithium diffusivities between lithium poor phases and lithium rich phases of the lithium tin alloys [27]. As shown in Ref [28], the lithium diffusivity in lithium poor phases (before LiSn) is about one order lower than that in the lithium rich phases. We can assume the lithium transport in the Sn foil electrode is a 1-D transport. From the surface of the Sn foil electrode (facing separator), the lithium concentration decreases gradually from high to 0. Due to the difference between the high diffusivity in lithium rich phases and the low diffusivity in lithium poor phases, it is favorable to form lithium rich

12

phases on the surface. At very low rate, the lithium poor phases could be detected on the surface and the plateaus could be visible. As shown in **Fig. 3a**, the three plateaus appear at the beginning of lithiation when the current density is 10 μA cm^{-2}. Since the XRD patterns in **Fig. 2b** do not show the existence of Li$_{22}$Sn$_5$ in points 1 and 2, other lithium rich phases are believed to exist before the appearance of Li$_{22}$Sn$_5$. These lithium rich phases cannot be detected by XRD. The possible reasons could be (1) they are amorphous; (2) they are too small or too transient to be detected [17]. As shown in **Fig. 2a**, the typical plateaus can appear in the 2nd lithiation. We believe that it is due to two reasons. The first reason is the significant surface area increase due to the pulverization, which results in low current density. The second reason is the inhomogeneity of the pulverized Sn foil. The lithium transport can no longer be considered as a 1-D transport.

To avoid the large volume expansion of the Sn foil electrode, the state of lithiation was controlled. Enhanced cycling performance can be achieved for more than 90 cycles by limiting the lithiation capacity of the Sn foil electrode at 1 mAh (2.04 mAh cm^{-2}), as shown in **Fig. 3b**. The CE starts at 68% in the initial cycle, and then increases to 96% in the second cycle. After that, it stays at a steady efficiency of >97% until the 90th cycle. By controlling the lithium uptake at 2.04 mAh cm^{-2}, the phase transitions to Li$_x$Sn$_y$ have been controlled to lithium poor phases (Li$_2$Sn$_5$ and LiSn). The lithium poor phases can only cause a small volume expansion for the Sn foil electrode. The relative volume V$_r$ is 1.22 for Li$_2$Sn$_5$, and 1.51 for LiSn. But the lithium rich phase (Li$_{22}$Sn$_5$) has a relative volume of 3.58, which causes the cracking[29]. This lithiation control avoids the transition to lithium rich phase, herein maintains the structural stability and enhances the cycling performance. In **Fig. 3c**, the XRD pattern at the end of

13

lithiation of 2.04 mAh cm^{-2} shows Li_2Sn_5 and LiSn phases, but no $Li_{22}Sn_5$ phase. Selected

voltage profiles in different cycles are shown in **Fig. 3d**. The initial discharge process shows a

single lithiation plateau at 0.4 V and the charge process shows two very short plateaus at 0.61 V

and 0.73 V and a long plateau at 0.8 V. In literature, the charge plateau at 0.61 V is considered

the transition from $Li_{22}Sn_5$ to LiSn. Our results show that this plateau could also be a transition

from other lithium rich phases to LiSn. The plateau at 0.73 V is the transition from LiSn to

Li_2Sn_5 and the plateau at 0.8 V is the transition from Li_2Sn_5 to Sn. The first charge profile can

also be explained by the different diffusivities between lithium rich phases and lithium poor

phases. Since the lithiation capacity was controlled, the major phases in the Sn foil electrode are

lithium poor phases (LiSn and Li_2Sn_5) after the first discharge. As indicated by the 0.4 V

discharge plateau, there should be some lithium rich phases on the surface of the Sn foil

electrode. At the beginning of the charge process, the lithium rich phases on the surface of Sn

foil are transferred to LiSn and then Li_2Sn_5 very quickly. The XRD pattern at the end of the first

charge shows the left Li_2Sn_5 and LiSn in the delithiation products, which explains the low CE of

the first cycle. The discharge profile in the 2nd cycle shows three plateaus. The first and the third

ones are short and the second one is long. The possible reason is the pulverization generated in

the first cycle. The second charge profile shows two plateaus. The plateau at 0.61 V does not

exist, which is in agreement with the short third plateau in the discharge profile, meaning the

existence of very little lithium rich phases. From the third cycle to the 54th cycle, the voltage

profiles have two lithiation plateaus and two delithiation plateaus, which means the phases are

changed between Sn and lithium poor phases (Li_2Sn_5 and LiSn). However, the profiles also show

that the length of the Sn/Li_2Sn_5 plateau keeps increasing and the length of the Li_2Sn_5/LiSn

plateau keeps decreasing for both discharge and charge profiles. It means that minor cracks

14

inside the Sn foil are generated and the surface area is increased continuously. The larger surface area promotes the formation of Li_2Sn_5. After the 54th cycle, the length of the Sn/Li_2Sn_5 plateau keeps decreasing and the length of the $Li_2Sn_5/LiSn$ plateau keeps increasing for both discharge and charge profiles. After the 78th cycle, the third plateau appears again, and its length continuously increases. After the 93rd cycle, the voltage profiles start to become unstable and have large voltage drop. We believe that it is because the pulverization become severe enough to generate isolated particles and the active surface area starts to decrease after the 54th cycle. After the 93rd cycle, the Sn foil electrode is completely pulverized and most of the Sn materials are isolated. The cycling performance demonstrates the cycling performance of Sn foil can be improved by controlling the state of lithiation. However, fracture still happens due to the ~50% volume change between Sn and LiSn. Eventually, pulverization will cause the failure of the Sn foil electrode after 90 cycles.

Sulfur has attracted much attention as a promising cathode material due to its high theoretical specific capacity (1672 mAh g^{-1}) [30, 31]. In this study, the sulfur cathode was prepared by using a solvent evaporation method applied by our group before [32]. The sulfur solution was prepared in carbon disulfide (CS_2) and injected into a CNT paper. Sulfur particles are evenly distributed within the CNT paper once CS_2 solvent is vaporized. The sulfur loading is 1.02 mg cm^{-2}, which is about 56% of the capacity of 0.7 cm^2 pre-lithiated Sn foil. The higher capacity of the Sn anode is to ensure the excess lithium resource for the possible waste of lithium due to polysulfides shuttle effect and the SEI formation. SEM and EDS were performed to examine the morphology and elemental distribution in the prepared electrodes, as shown in **Figs. 4a, b** and **c**, respectively. The SEM image in **Fig. 4a** shows the structural morphology of the prepared

15

sulfur/CNT electrode. It can be seen that a lot of regular sulfur particles were deposited in the voids of the CNT paper. Under the detection of SEM, the sulfur particles are in nanoscale. The EDS in **Figs. 4b and c** reveal the carbon element in the CNT paper network structure and the uniform distribution of sulfur element in the electrode. The electrode prepared by this method promises reliable and controllable deposition of sulfur in CNT paper. The cycling performance of the S cathode at $C/5$ is shown in **Fig. 4d**. The sulfur cathode delivers 1225 mAh g^{-1} in the 1st cycle, and then the capacity increases to 1312 mAh g^{-1} in the 2nd cycle. After 100 cycles, the specific capacity is stabilized at 994 mAh g^{-1}. The result demonstrates that the sulfur cathode prepared by this method is robust in retaining active material thus offering stable cycling performance. Selected voltage profiles for the sulfur cathode are shown in **Fig. 4e**. The cell is discharged to 1.7 V to avoid the LiNO$_3$ reduction reactions at low potential ($\leq$1.65 V). The sulfur cathode has two visible plateaus in the discharge and two plateaus in the charge. It can be observed that the cell polarization (the voltage difference between the first charge voltage plateau and the second discharge voltage plateau) is 0.65 V in 2nd cycle. Then it continuously decreases to lower than 0.3 V during cycling. **Fig. 4f** shows the CV of the Li-S cell. There are two cathodic peaks at 2.37 V and 2.05 V corresponding to the reduction reactions of sulfur to low-order polysulfides and low-order polysulfides to Li$_2$S, and two distinguishable anodic peaks at 2.28 V and 2.41 V, which indicate the transition of Li$_2$S to high-order polysulfides/sulfur [33]. The cell exhibits a stable CV profile over 10 cycles without decay of peak intensity.

To set up a S-Sn full cell, the Sn foil electrode was cycled with 1.5 mAh capacity limitation (2.1 mAh cm^{-2}) for 4 cycles for pre-lithiation. As shown in **Fig. 5a**, the foil still maintains its structural stability after pre-lithiation, due to the limited lithiation capacity, low cycling current

16

(0.03 C), and homogenous lithiation process. The Sn foil anode from the cycled S-Sn full cell was also obtained at discharged state after 10 cycles, as shown in **Fig. 5b**. Compared to the image shown in **Fig. 5a**, it did not have significant changes after 10 cycles in the S-Sn full cell. SEM was performed to investigate the anode extracted from the full cell at discharged state, as shown in **Fig. 5c**. In this high magnification, it can be observed that the anode surface has formed porous structures. It means that fracturing still happens even the lithium uptake is limited. The EDS map of nitrogen species, oxygen species and tin species is shown in **Figs. 5d-g**. The nitrogen and oxygen elements could be from the passivation layer from $LiNO_3$ and the SEI layer. They could also be from the residual lithium salts. The EDS mapping result shows that some of the electrode areas are not covered by the passivation layer. We believe that it is due to the volume change of Sn electrode during lithiation/delithiation processes.

When sulfur cathode is coupled with the lithiated Sn anode and cycled at $C/2$, the cycling performance in **Fig. 6a** is observed, with an inset picture showing the schematic construction of the S-Sn full cell. The full cell has an initial capacity of 1143 mAh g^{-1} in the 1st cycle, and then yield the capacity of 960 mAh g^{-1} in the 2nd cycle. The full cell exhibits stable cycling performance with remaining reversible capacity of 552 mAh g^{-1} after 100 cycles. The full cell has an initial CE of 64% and retaining efficiency of >82%. Although the volume change of Sn keeps exposing fresh Sn surfaces and leads to new SEI formation, the CE shown in **Fig. 3c** is higher than 96%. The low CE shown in the S-Sn full cell means that $LiNO_3$ is not as effective as in the Li-S cell to prevent the shuttle effect. The Sn surface is not completely covered by the passivation layer as shown in **Fig. 5**. The full cell operating voltage profile is shown in **Fig. 6b**. During discharge, two plateaus are shown. The first reduction plateau is at 1.7 V which is

17

corresponding to the combination of formation from sulfur to low-order polysulfides and lithium extraction from lithiated Sn anode. The second discharge plateau is at 1.36 V, which is attributed to the formation of Li_2S and low-order lithiated Sn. The charge process is a highly reversible process with two charge plateaus around 1.6 V and 1.8 V, respectively. The first cycle has a long charge process, which results in a low CE. The capacity fade during conversion process is due to the consumption of lithium upon prolonged cycling and shuttle effect of high order polysulfides. The CV for the S-Sn full cell is shown in **Fig. 6c**. There are two cathodic peaks at 1.65 and 1.37 V corresponding to the reduction reactions of sulfur to low-order polysulfides and low-order polysulfides to Li_2S. The second cathodic peak is obviously the overlap of two peaks with a miniature peak at 1.3 V. The peak could be attributed to the phase transform of Sn anode leading the voltage change. In the anodic scan, two distinguishable peaks are observed at 1.74 and 1.79 V, which indicate the transition from Li_2S to high-order polysulfides/S as a conversion process. The cell exhibits a stable CV profile over 10 cycles without large decay of peak intensity. The cycling result of S-Sn full cell demonstrates that shuttle effect of polysulfides is still a major issue. Polysulfides can react with lithium in the lithium tin alloy and $LiNO_3$ cannot form a seamless passivation layer to protect lithium tin alloy surface. The performance of such a system could be further improved by applying high loading carbon interlayers [34, 35], modification of polysulfide carbon host[36, 37], and other functionalized materials such as graphene and polymers to contain lithium polysulfides in the cathode [38-42].

4.   Conclusion

In this work, Sn foil has been studied as a high capacity anode for lithium batteries. By controlling the degree of lithium uptake, a stable long cycling life can be obtained for Sn foil

anode. Ex-situ XRD results and lithiation/delithiation profiles show that the different lithium diffusivity between lithium poor phases and lithium rich phases has significant impact on the electrochemical performance of Sn foil. A S-Sn full cell has been developed by using pre-lithiated Sn foil anode and S/CNT cathode and it shows high specific capacity. However, the CE is lower than 90% mainly due to the shuttle effect of polysulfides. $LiNO_3$ is not effective in forming passivation layer on the lithiated Sn anode as it is in the lithium sulfur batteries. New approach needs to be developed to prevent the shuttle effect. Although the shuttle effect is not evaded from the full cell system, it provides a concept and potential for further studying the S-Sn full cell system.

19

References

[1] A.R. Kamali, D.J. Fray, Tin-based materials as advanced anode materials for lithium ion batteries: a review, Rev. Adv. Mater. Sci, 27 (2011) 14-24.

[2] S. Goriparti, E. Miele, F. De Angelis, E. Di Fabrizio, R.P. Zaccaria, C. Capiglia, Review on recent progress of nanostructured anode materials for Li-ion batteries, J. Power Sources, 257 (2014) 421-443.

[3] G. Ehrlich, C. Durand, X. Chen, T. Hugener, F. Spiess, S. Suib, Metallic negative electrode materials for rechargeable nonaqueous batteries, J. Electrochem. Soc., 147 (2000) 886-891.

[4] L. Beaulieu, K. Eberman, R. Turner, L. Krause, J. Dahn, Colossal reversible volume changes in lithium alloys, Electrochem. Solid-State Lett., 4 (2001) A137-A140.

[5] M. Zhang, T. Wang, G. Cao, Promises and challenges of tin-based compounds as anode materials for lithium-ion batteries, Int. Mater. Rev., 60 (2015) 330-352.

[6] H.X. Dang, K.C. Klavetter, M.L. Meyerson, A. Heller, C.B. Mullins, Tin microparticles for a lithium ion battery anode with enhanced cycling stability and efficiency derived from Se-doping, J. Mater. Chem. A, 3 (2015) 13500-13506.

[7] F. Xin, X. Wang, J. Bai, W. Wen, H. Tian, C. Wang, W. Han, A lithiation/delithiation mechanism of monodispersed MSn 5 (M= Fe, Co and FeCo) nanospheres, J. Mater. Chem. A, 3 (2015) 7170-7178.

[8] Z. Zhu, S. Wang, J. Du, Q. Jin, T. Zhang, F. Cheng, J. Chen, Ultrasmall Sn nanoparticles embedded in nitrogen-doped porous carbon as high-performance anode for lithium-ion batteries, Nano Lett., 14 (2013) 153-157.

[9] L. Bazin, S. Mitra, P.L. Taberna, P. Poizot, M. Gressier, M.J. Menu, A. Barnabé, P. Simon, J.-M. Tarascon, High rate capability pure Sn-based nano-architectured electrode assembly for rechargeable lithium batteries, J. Power Sources, 188 (2009) 578-582.

[10] Y. Liu, N. Zhang, L. Jiao, Z. Tao, J. Chen, Ultrasmall Sn Nanoparticles Embedded in Carbon as High-Performance Anode for Sodium-Ion Batteries, Adv. Funct. Mater., 25 (2015) 214-220.

[11] Y. Yu, Q. Yang, D. Teng, X. Yang, S. Ryu, Reticular Sn nanoparticle-dispersed PAN-based carbon nanofibers for anode material in rechargeable lithium-ion batteries, Electrochem. Commun., 12 (2010) 1187-1190.

[12] Y. Xu, Q. Liu, Y. Zhu, Y. Liu, A. Langrock, M.R. Zachariah, C. Wang, Uniform nano-Sn/C composite anodes for lithium ion batteries, Nano Lett., 13 (2013) 470-474.

[13] J. Luo, X. Zhao, J. Wu, H.D. Jang, H.H. Kung, J. Huang, Crumpled graphene-encapsulated Si nanoparticles for lithium ion battery anodes, J. Phys. Chem. Lett., 3 (2012) 1824-1829.

[14] H. Mukaibo, T. Sumi, T. Yokoshima, T. Momma, T. Osaka, Electrodeposited Sn-Ni alloy film as a high capacity anode material for lithium-ion secondary batteries, Electrochem. Solid-State Lett., 6 (2003) A218-A220.

[15] X.-L. Wang, W.-Q. Han, J. Chen, J. Graetz, Single-crystal intermetallic M− Sn (M= Fe, Cu, Co, Ni) nanospheres as negative electrodes for lithium-ion batteries, ACS Appl. Mater. Interfaces, 2 (2010) 1548-1551.

[16] M. Marcinek, L. Hardwick, T. Richardson, X. Song, R. Kostecki, Microwave plasma chemical vapor deposition of nano-structured Sn/C composite thin-film anodes for Li-ion batteries, J. Power Sources, 173 (2007) 965-971.

[17] K.J. Rhodes, R. Meisner, M. Kirkham, N. Dudney, C. Daniel, In situ XRD of thin film tin electrodes for lithium ion batteries, J. Electrochem. Soc., 159 (2012) A294-A299.

[18] J. Hassoun, S. Panero, P. Reale, B. Scrosati, A new type of lithium-ion battery based on tin electroplated negative electrodes, Int. J. Electrochem. Sci, 1 (2006) 110-121.

[19] N. Tamura, R. Ohshita, M. Fujimoto, S. Fujitani, M. Kamino, I. Yonezu, Study on the anode behavior of Sn and Sn–Cu alloy thin-film electrodes, J. Power Sources, 107 (2002) 48-55.

[20] S. Yang, P.Y. Zavalij, M.S. Whittingham, Anodes for lithium batteries: tin revisited, Electrochem. Commun., 5 (2003) 587-590.

[21] K.J. Kreder III, B.T. Heligman, A. Manthiram, Interdigitated Eutectic Alloy Foil Anodes for Rechargeable Batteries, ACS Energy Lett., 2 (2017) 2422-2423.

[22] J. Hassoun, J. Kim, D.-J. Lee, H.-G. Jung, S.-M. Lee, Y.-K. Sun, B. Scrosati, A contribution to the progress of high energy batteries: A metal-free, lithium-ion, silicon–sulfur battery, J. Power Sources, 202 (2012) 308-313.

[23] R. Elazari, G. Salitra, G. Gershinsky, A. Garsuch, A. Panchenko, D. Aurbach, Rechargeable lithiated silicon–sulfur (SLS) battery prototypes, Electrochem. Commun., 14 (2012) 21-24.

[24] Y. Yang, M.T. McDowell, A. Jackson, J.J. Cha, S.S. Hong, Y. Cui, New nanostructured Li2S/silicon rechargeable battery with high specific energy, Nano Lett., 10 (2010) 1486-1491.

[25] S.M. Wood, E.J. Powell, A. Heller, C.B. Mullins, Lithiation and delithiation of lead sulfide (PbS), J. Electrochem. Soc, 162 (2015) A1182-A1185.

[26] J. Hassoun, B. Scrosati, A High-Performance Polymer Tin Sulfur Lithium Ion Battery, Angew. Chem., Int. Ed., 49 (2010) 2371-2374.

[27] J. Yang, Y. Takeda, N. Imanishi, O. Yamamoto, Ultrafine Sn and SnSb0.14 powders for lithium storage matrices in lithium-ion batteries, Journal of the Electrochemical Society, 146 (1999) 4009-4013.

[28] M. Winter, J.O. Besenhard, Electrochemical lithiation of tin and tin-based intermetallics and composites, Electrochim. Acta, 45 (1999) 31-50.

[29] T. Ichitsubo, S. Yukitani, K. Hirai, S. Yagi, T. Uda, E. Matsubara, Mechanical-energy influences to electrochemical phenomena in lithium-ion batteries, J. Mater. Chem., 21 (2011) 2701-2708.

[30] P.G. Bruce, S.A. Freunberger, L.J. Hardwick, J.-M. Tarascon, Li–O 2 and Li–S batteries with high energy storage, Nat. Mater., 11 (2012) 19.

[31] A. Manthiram, Y. Fu, S.-H. Chung, C. Zu, Y.-S. Su, Rechargeable lithium–sulfur batteries, Chem. Rev., 114 (2014) 11751-11787.

[32] Y. Cui, J.D. Ackerson, Y. Ma, A. Bhargav, J.A. Karty, W. Guo, L. Zhu, Y. Fu, Phenyl Selenosulfides as Cathode Materials for Rechargeable Lithium Batteries, Adv. Funct. Mater., (2018) 1801791.

[33] Y. Fu, Y.S. Su, A. Manthiram, Highly Reversible Lithium/Dissolved Polysulfide Batteries with Carbon Nanotube Electrodes, Angew. Chem., Int. Ed., 52 (2013) 6930-6935.

[34] Y.-S. Su, A. Manthiram, Lithium–sulphur batteries with a microporous carbon paper as a bifunctional interlayer, Nat. Commun., 3 (2012) 1166.

[35] J. Balach, T. Jaumann, M. Klose, S. Oswald, J. Eckert, L. Giebeler, Functional Mesoporous Carbon-Coated Separator for Long-Life, High-Energy Lithium–Sulfur Batteries, Adv. Funct. Mater., 25 (2015) 5285-5291.

[36] C.J. Hart, M. Cuisinier, X. Liang, D. Kundu, A. Garsuch, L.F. Nazar, Rational design of sulphur host materials for Li–S batteries: correlating lithium polysulphide adsorptivity and self-discharge capacity loss, Chem. Commun., 51 (2015) 2308-2311.

21

[37] H. Xu, L. Qie, A. Manthiram, An integrally-designed, flexible polysulfide host for high-performance lithium-sulfur batteries with stabilized lithium-metal anode, Nano Energy, 26 (2016) 224-232.

[38] Z. Zhang, L.L. Kong, S. Liu, G.R. Li, X.P. Gao, A High-Efficiency Sulfur/Carbon Composite Based on 3D Graphene Nanosheet@ Carbon Nanotube Matrix as Cathode for Lithium–Sulfur Battery, Adv. Energy Mater., 7 (2017) 1602543.

[39] J. Song, Z. Yu, M.L. Gordin, D. Wang, Advanced sulfur cathode enabled by highly crumpled nitrogen-doped graphene sheets for high-energy-density lithium–sulfur batteries, Nano Lett., 16 (2016) 864-870.

[40] J. Liu, T. Qian, M. Wang, X. Liu, N. Xu, Y. You, C. Yan, Molecularly imprinted polymer enables high-efficiency recognition and trapping lithium polysulfides for stable lithium sulfur battery, Nano Lett., 17 (2017) 5064-5070.

[41] Y. Cui, Y. Fu, Enhanced Cyclability of Li/Polysulfide Batteries by a Polymer-Modified Carbon Paper Current Collector, ACS Appl. Mater. Interfaces, 7 (2015) 20369-20376.

[42] P. Xiao, F. Bu, G. Yang, Y. Zhang, Y. Xu, Integration of graphene, nano sulfur, and conducting polymer into compact, flexible lithium–sulfur battery cathodes with ultrahigh volumetric capacity and superior cycling stability for foldable devices, Adv. Mater., 29 (2017) 1703324.
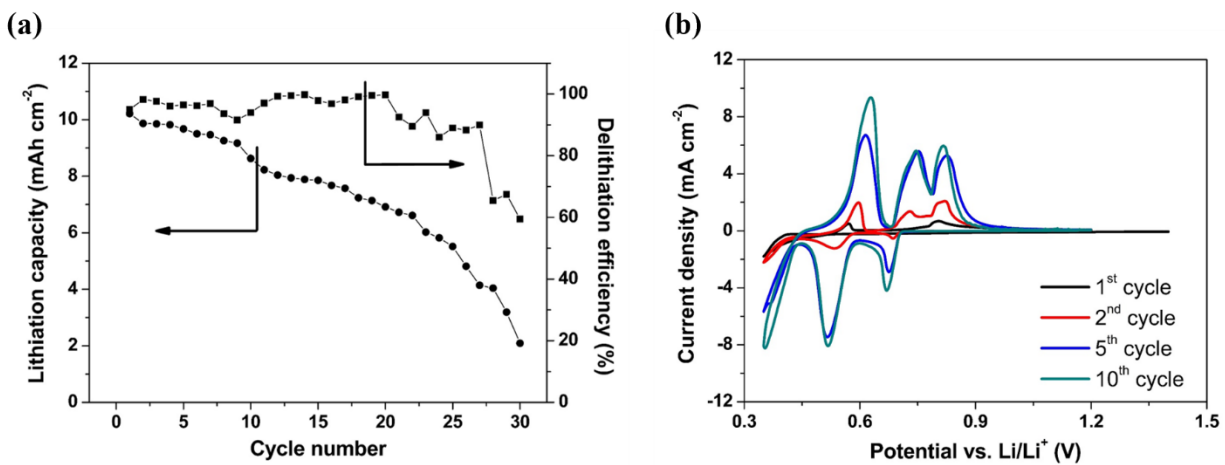
Fig. 1. (a) Cycling performance of the Sn foil at 0.03 C rate, (b) cyclic voltammogram of the 1st, 2nd, 5th, and 10th cycles.
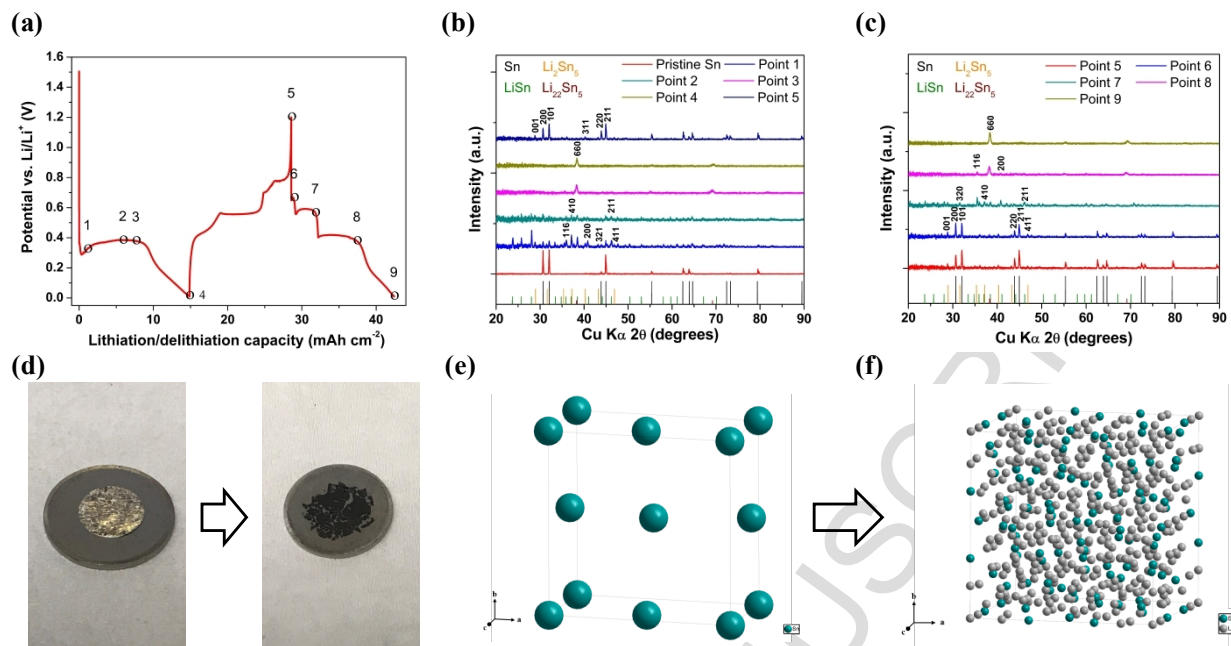
Fig. 2. (a) Voltage-capacity profile showing collected XRD patterns points, XRD patterns of the Sn foil in (b) the 1st cycle and (c) the 2nd cycle, (d) pictures showing the morphological changes from pristine Sn foil to lithiated product, the atomic structures of (e) Sn and (f) $Li_{22}Sn_5$. Tin and lithium atoms are represented in green and gray, respectively.

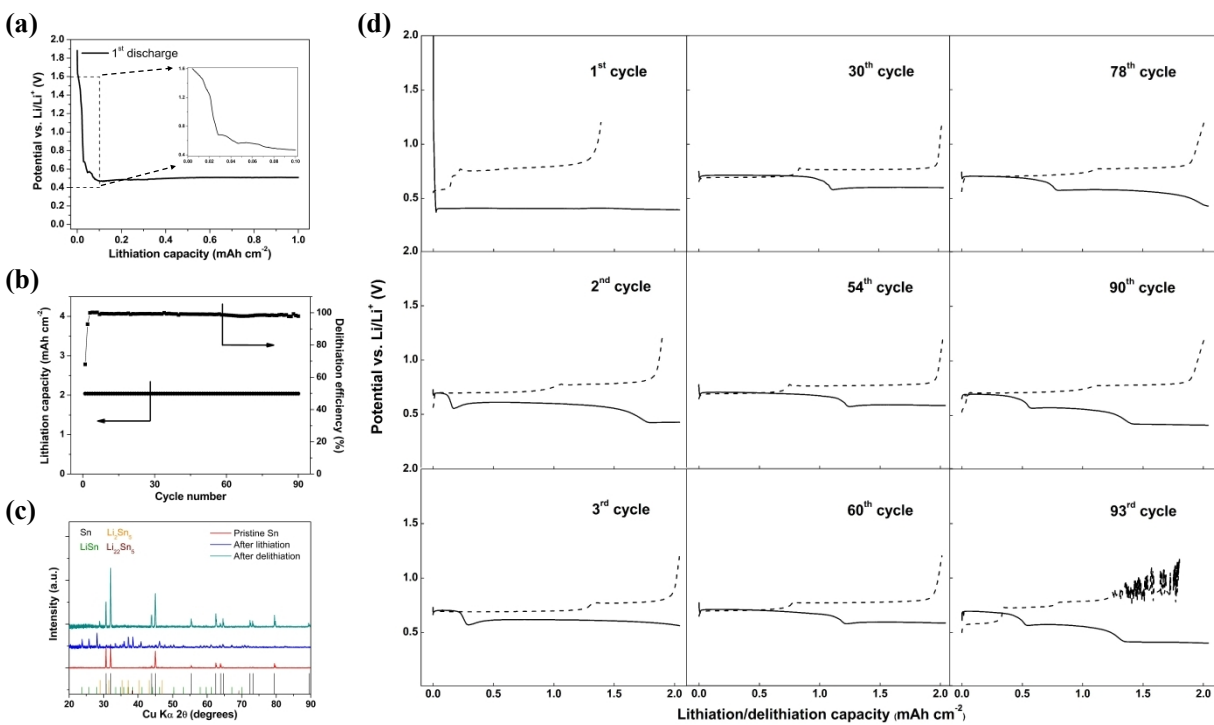Fig. 3. (a) Voltage-capacity profile of the Sn foil at 10 μA cm^{-2} current density, (b) cycling performance, (c) XRD patterns in the 1st cycle and (d) selected voltage-capacity profiles of the Sn foil at 0.03 C rate with lithiation capacity limit of 2.04 mAh cm^{-2}.
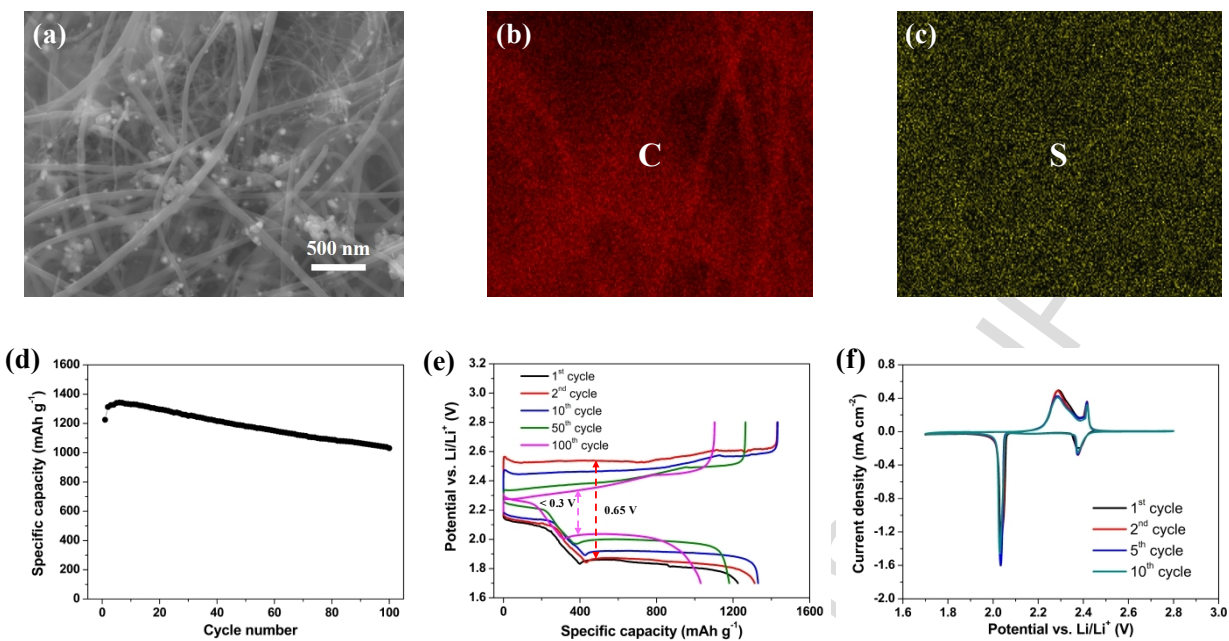
Fig. 4. (a) SEM image and (b-c) EDS scan for carbon and sulfur, (d) cycling performance, (e) selected voltage-capacity profiles, and (f) cyclic voltammogram of the sulfur cathode.
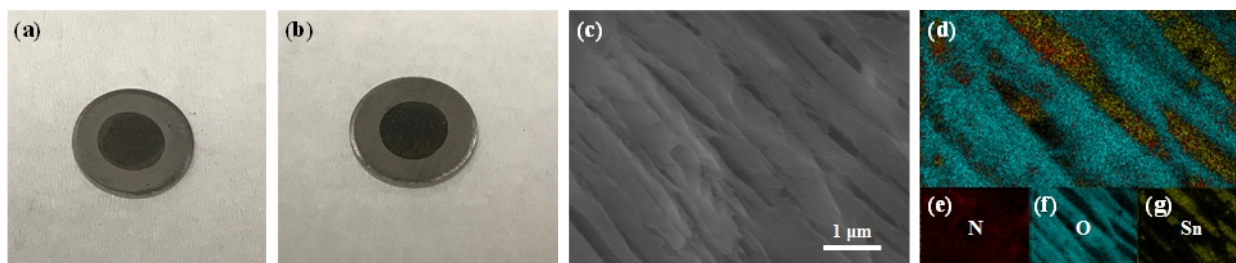
Fig. 5. (a) Picture of the Sn foil after pre-lithiation, (b) picture of the Sn foil, (c) SEM image and (d-g) EDS scan for overlapping, nitrogen, oxygen and tin for the Sn foil anode at discharged state after 10 cycles in the S-Sn full cell.
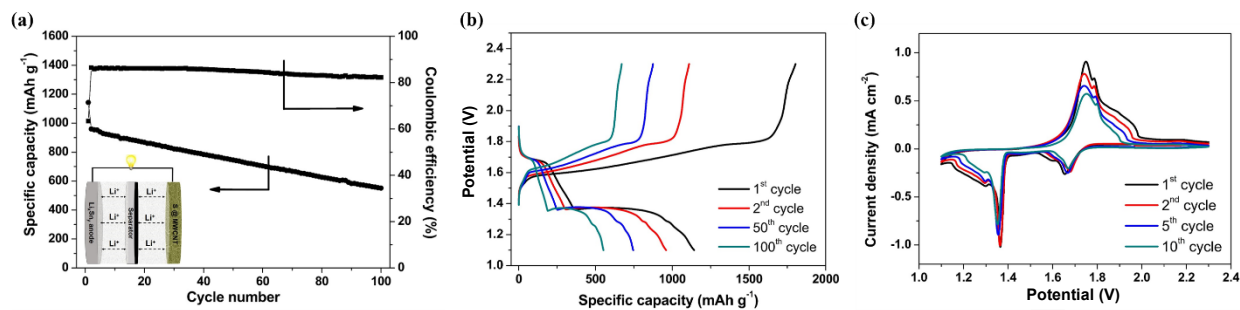
Fig. 6. (a) Cycling performance with an inset schematic of construction of the S-Sn full cell, (b) selected voltage-capacity profiles and (c) cyclic voltammogram of the S-Sn full cell.

28

EA # 18-5144

RESPONSE TO REVIEWERS' COMMENTS

REVIEWER 1:

Comment 1: *How to control lithiation capacity for pre-lithiated Sn foil? How to ensure the reproducibility of this critical point to obtain good electrochemical performance and keep the electrode uncracked for pre-lithiated Sn foil?*

Response to comment 1:

The Sn foil was pre-lithiated in a Sn/Li metal half cell. The full lithiation capacity of the Sn foil was calculated by its weight and the theoretical capacity to form $Li_{22}Sn_5$. The lithiation capacity was controlled by setting the "discharge capacity limit" in the Arbin BT2000 battery cycler during the galvanostatic lithiation process.

Compared to the Sn particle-based composite electrode, the Sn foil can be considered homogenous during the lithiation process. In the particle-based composite electrode, different Sn particles could have different lithiation capacity during the pre-lithiation process. It is difficult to ensure the reproducibility of the critical point for all the Sn particles. However, the Sn foil electrode does not have this problem due to the homogenous lithiation process. In addition, the cycling current was very low (0.03 C) during the pre-lithiation process. The pre-lithiation capacity can be reproduced in this work. In Fig. 5a, the picture shows the maintained structural stability after pre-lithiation. More explanations have been added for Fig. 5a on pages 16 - 17.

Comment 2: *What is mechanism of pre-lithiated Sn foil anode to keep enhanced electrochemical*

29

performance and meanwhile inhibit volume expansion of Sn during Li-ion insertion-deinsertion process?

Response to comment 2:

By controlling the lithiation capacity, the phase transitions to Li_xSn_y have been controlled to lithium poor phases (Li_2Sn_5 and LiSn). This control avoids the transition to lithium rich phase ($Li_{22}Sn_5$). The lithium poor phases can only cause a small volume expansion for the Sn foil. The relative volume V_r is 1.22 for Li_2Sn_5, and 1.51 for LiSn. But the lithium rich phase $Li_{22}Sn_5$ has a relative volume of 3.58, which causes the cracking [1]. Therefore, this lithiation capacity control maintains the structural stability and enhances the electrochemical performance. Related explanations have been added on page 13 in the manuscript.

Comment 3: What is the phase of Sn foil when it is pre-lithiated at reasonable content? Why this phase can restrain the electrode from strong volume expansion?

Response to comment 3:

After the pre-lithiation, the phases of the Sn foil are mainly Li_2Sn_5 and LiSn (lithium poor phases). The lithium poor phases can only cause small volume expansions. Therefore, the capacity control can avoid the large volume expansion.

30

REVIEWER 2:

Comment 1: The XRD patterns of the Sn foil in Fig. 2a, b are not clearness. Please use different colours to distinct the Li22Sn5, Li2Sn5, LiSn, Sn.

Response to comment 1:

The XRD patterns have been clarified by using different colors and length, according to this suggestion.

Comment 2: In Fig. 2a, at the end of the single lithiation plateau (point 3), the mainly present phase is detected to be Li22Sn5. Why in Fig. 3c, the XRD pattern at the end of lithiation of 1 mAh shows Li2Sn5 and LiSn phases? but no Li22Sn5 phase.

Response to comment 2:

The Sn foil at point 3 in Fig. 2a has a lithiation capacity of 8 mAh cm^{-2}, which is close to the end of full lithiation. This large lithiation capacity makes the phase transition to lithium rich phase ($Li_{22}Sn_5$). However, in Fig. 3c, the lithiation capacity was controlled to 2.04 mAh cm^{-2}, which is at the early stage of lithiation. The limited lithiation capacity makes the phase transitions only to lithium poor phases (Li_2Sn_5 and LiSn). More explanations have been added for Fig. 3 on page 13.

Comment 3: In the S-Sn full cell, the author should explain why sulfur loading is 1.02 mg cm-2, which can provide a comparable capacity to that of the Sn anode?

Response to comment 3:

In this study, the 1.02 mg cm^{-2} sulfur loading provided 0.82 mAh capacity and the pre-lithiated Sn foil provided 1.47 mAh capacity. The capacity of Sn anode is higher than S cathode because of the consideration of the wasted lithium resource due to the polysulfides shuttle effect and the SEI formation. Although the Sn foil have controlled to a limited capacity with relatively low volume expansion, the SEI formation is likely to happen during each charging process. More explanations have been added at related position on page 15 in the manuscript.

Comment 4: The authors claimed the Sn foil becomes dark black and cracked into pieces in Fig. 2d. However, is there a similar problem during the S-Sn full cell cycling?

Response to comment 4:

In Fig. 2d after one cycle of full lithiation, the Sn foil has cracked into pieces. During the S-Sn full cell cycling, the cycling capacity was controlled to avoid the large volume expansion. A picture of the Sn foil after 10 cycles in the S-Sn full cell has been added to Fig. 5b. After 10 cycles, the Sn foil only has limited volume expansions, but maintains the structural stability. More explanations have been added on pages 16 – 17 in the manuscript.

Comment 5: The sputtered Sn foil was cut into 0.49 cm2 discs (D = 7.9 mm, including 9.5 mg Sn each) for Sn half-cell test, and 0.7cm2 discs (D = 9.5 mm, including 13.5 mg Sn each) for pre-

lithiation as the lithium source in S-Sn full cells. Please provide some solid information about the difference.

Response to comment 5:

When making Li-Sn half cells in coin cells, the size of the Sn foil can be from 0.2 cm² to more than 1 cm². Current density and the size of lithium metal anode can be calculated and adjusted based on the size of the Sn foil. There is not a special reason to select 0.49 cm². 0.49 cm² is the size of the puncher that our group use for cutting our battery electrodes.

In the full cell system, 0.7 cm² Sn foil was used. There are two reasons to use 0.7 cm² Sn foil instead of 0.49 cm² Sn foil. The first reason is that we want to make the capacity of Sn foil anode larger than the S cathode (0.49 cm²). The second reason is that we want to make the area of Sn anode larger than S cathode. In this case, the capacity of S cathode can be fully utilized.

Comment 6: Galvanostatic discharge/charge and cyclic voltammogram upon cycling in Fig. 4d should be provided. And explain why chose the cyclic voltammogram of the S-Sn full cell from 1.1V to 2.3V.

Response to comment 6:

Selected voltage profiles and CV profiles for sulfur cathode have been added to Figs. 4e and f. More explanations have been added on page 16. In the full cell system, the potential of the 1st plateau is the combination of sulfur's first reduction potential and tin's first oxidation potential, theoretically it is 2.35-0.45 = 1.9 V. The potential of the 2nd plateau in full cell is the combination of sulfur's 2nd reduction potential and tin's 2nd oxidation potential, theoretically it is 2.1-0.7=1.4

V. The same calculation method is used for the reversible process. Therefore, the cycling

potential range for full cell system is set up between 1.1-2.3 V.

Comment 7: *Please check the language throughout the text. There are a few grammar errors.*

Response to comment 7:

The text has been checked. The grammar errors have been corrected.

Comment 8: *The references should keep the same format. And there are a lot of questions, the*

author should take it seriously.

Response to comment 8:

The format for references has been corrected.

1. T. Ichitsubo, S. Yukitani, K. Hirai, S. Yagi, T. Uda, E. Matsubara, J. Mater. Chem., 21
    (2011) 2701-2708.